Boundary-Layer Meteorology (2020) 175:1–23
https://doi.org/10.1007/s10546-019-00491-y

RESEARCH ARTICLE

Turbulent Heat and Momentum Exchange in Nocturnal Drainage Flow Through a Sloped Vineyard

Kelsey A. Everard[1] · **Holly J. Oldroyd**[2] · **Andreas Christen**[3]

Received: 10 August 2018 / Accepted: 26 November 2019 / Published online: 28 January 2020

Abstract

High-frequency measurements are available at five heights within and above a row-gap trellised vineyard located on a 7° slope in the Southern Okanagan Valley, British Columbia, Canada. During a 3-week campaign in July 2016, approximately 17% of the nocturnal conditions exhibit drainage flow along the local slope. Drainage conditions are characterized by temperature inversions beginning around $z/h_c = 0.39$, where z is the height above ground level (a.g.l.) and h_c is the canopy height (2.3 m a.g.l.), and near-surface lapses. Changes in the sign of the streamwise momentum flux suggest the presence of a jet maximum around $z/h_c = 1.65$, while a weak inflection point is observed near the canopy top, suggesting dynamical influences from both the drainage layer and canopy layer on the turbulent flow field. The largest observed fluxes in both the streamwise momentum flux and the turbulent sensible heat flux are near the top of the canopy, consistent with the location of the inflection point. Calculated two-point length scales from along-slope distributed temperature measurements reveal that turbulent structures are smallest near the canopy top. Conditional sampling of the three-dimensional velocity components and temperature indicate that a large fraction of canopy-layer transport is driven by canopy top turbulence, with sweeps dominating over ejections, particularly at $z/h_c = 0.65$.

Keywords Canopy layer · Coherent structures · Nocturnal boundary layer · Two-point statistics · Turbulence · Quadrant analysis

1 Introduction

An understanding of the local wind and temperature fields within a vegetated canopy is of great importance for the mitigation of frost damage and the spread of plant disease in agricultural crops (Mahaffee and Stoll 2016), and to the development of parametrizations

✉ Kelsey A. Everard
kelsey.everard@alumni.ubc.ca

[1] Department of Civil Engineering, The University of British Columbia, Vancouver, Canada

[2] Department of Civil and Environmental Engineering, University of California at Davis, Davis, USA

[3] Faculty of Environment and Natural Resources, Chair of Environmental Meteorology, University of Freiburg, Freiburg, Germany

for the surface–atmosphere exchange of heat, momentum, and scalars in models. Extensive research into the mean and turbulent wind fields within the roughness sublayer (RSL), which extends from the ground surface to approximately two to five times the canopy height, h_c (e.g., Raupach et al. 1991; Finnigan 2000; Oke et al. 2017), has allowed for the emergence of a general understanding of canopy flow for homogeneous plant canopies over flat, horizontal terrain under neutral atmospheric static stability.

For example, it is well known that statically near-neutral atmospheric flow dynamics within the RSL for homogeneous plant canopies over flat terrain are analogous to the dynamics of plane mixing layers (Raupach et al. 1996; Finnigan 2000; Finnigan et al. 2009). Flow is rapidly slowed with depth into the canopy by the effects of canopy drag, resulting in an inflection point near h_c in the vertical mean flow profile (e.g., Raupach et al. 1996). As with the plane mixing layer, flow in the vegetated RSL is hydrodynamically unstable in the region of this velocity inflection point, and it is in this region where canopy-scale coherent structures are generated (e.g., Raupach et al. 1996; Finnigan 2000). These large structures are observed as coherent turbulent motions in the RSL, namely, sweeps and ejections, and are responsible for a large part of the total RSL surface fluxes (e.g., Thomas and Foken 2007a). While this characterization is observed over a wide range of canopies (e.g., Gao et al. 1989; Shaw et al. 1995; Thomas and Foken 2007a; Chahine et al. 2014), there are a number of factors that are known to affect the mean and turbulent dynamics within the vegetated RSL, including atmospheric stability (e.g., Leclerc et al. 1990; Launiainen et al. 2007; Li and Bou-Zeid 2011; Dupont and Patton 2012), canopy density (e.g., Poggi et al. 2004; Dupont and Brunet 2008), canopy architecture and row orientation with respect to the mean flow (Miller et al. 2017), surface inhomogeneities such as the sharp transitions characteristic of canopy edges (e.g., Irvine et al. 1997), and complex terrain (e.g., Poggi and Katul 2007; Thomas and Foken 2007b).

Of all of the complexities, the effects of canopy density are perhaps the most explored (e.g., Poggi et al. 2004; Dupont and Brunet 2008; Miller et al. 2017). Whether a canopy is considered dense or sparse depends not only on the leaf area density itself, but for canopies with a preferred orientation like those typical of agricultural canopies, also on the orientation of the canopy with respect to the mean outer-canopy flow (Miller et al. 2017). While plane mixing-layer-like dynamics are typically well observed in the vegetated RSL, the strength of the analogy weakens with increasing canopy sparsity, and ceases to be applicable for sufficiently sparse canopies (e.g., Dupont and Brunet 2008). Not only is canopy density known to affect the behaviour of larger coherent structures, but also the contribution of dispersive fluxes to the total RSL flux (e.g., Poggi and Katul 2008; Bailey and Stoll 2013).

In comparison to the body of work that has focused on variations in canopy density, very little attention has been given to the combined effect of complex terrain and atmospheric stability, which can lead to thermo-topographically forced flows (e.g., Whiteman 2000), on vegetated RSL dynamics. Aside from the vast body of literature focussed almost exclusively on the effects of drainage flow on advection and budget closures at forested FLUXNET sites (e.g., Aubinet et al. 2003; Turnipseed et al. 2003; Aubinet 2008; Belcher et al. 2008; Thomas 2011), and the few studies that consider the effects of a canopy on the behaviour of thermo-topographic flows (e.g., Garrett 1983; Chen and Yi 2012; Oldroyd et al. 2014), to our knowledge, the only study to explore RSL flow dynamics specifically within a sloped vineyard was that by Francone et al. (2012). However, while Francone et al. (2012) explicitly investigate RSL flow dynamics under conditions conducive to drainage flow (static stability and sloping terrain), they make no mention of possible drainage and rely on single point-measurements that are inadequate in resolving the behaviour of the mean and turbulent dynamics associated with drainage flows. This prevented them from fully exploring the effects that stability and terrain slope may have on the behaviour of vegetated RSL dynamics.

Drainage flow conditions arise over regions of sloping terrain given sufficient night-time radiative surface cooling, and sufficiently weak synoptic pressure gradients (e.g., Whiteman 2000). While there exists a strong body of work that has elucidated the theoretical nature of drainage under idealized conditions (Fleagle 1950; Mahrt 1982; Whiteman 2000), and a large number of studies that have furthered our understanding of drainage (or katabatic) flows observed over real Earth surfaces (e.g., Gudiksen et al. 1992; Horst and Doran 1986; Oldroyd et al. 2014; Grachev et al. 2016; Oldroyd et al. 2016), much less attention has been given to resolving the interaction of these flows with vegetation. Drainage flows themselves present interesting dynamics without the interaction of a canopy, such as a near-surface jet maximum that indicates a change in the direction of mean surface-normal momentum fluxes in the near-jet peak region (e.g., Oldroyd et al. 2014; Grachev et al. 2016), and the potential for buoyant turbulence kinetic energy (TKE, e) production via slope-parallel buoyancy fluxes (Horst and Doran 1988; Denby 1999; Oldroyd et al. 2016). With the presence of a canopy, the dynamics become more complex as added mechanical drag and canopy–atmosphere heat transfer potentially alters the behaviour of a drainage flow and thus the continued interaction of the two flow types.

Within this context, the interaction of nocturnal drainage flow with an organized, trellised canopy (typical of vineyards) presents an interesting and pertinent case to consider. For instance, drainage flow has the potential to impact vineyard management practices, and even influence considerations on the location of new crops, making an understanding on the behaviour of canopy–atmosphere exchange during night-time stability important. Few investigations have considered this particular type of non-homogeneous canopy (e.g., Francone et al. 2012; Chahine et al. 2014; Miller et al. 2015, 2017), revealing a complex relationship between canopy organization and turbulent and mean flow dynamics. Canopies with a row-gap organization can behave as either a dense or a sparse canopy, depending upon the approaching wind angle (Miller et al. 2017). Thus, given the fixed orientation of trellised canopies (once planted) and the predictable nature of drainage flows in terms of general flow direction, understanding how drainage flow interacts with a trellised canopy can be widely beneficial to fixed-row-gap agricultural practices on or near topographical slopes. A natural extension of research to date is an investigation into the case of static atmospheric stability over a slope in a vineyard, with explicit consideration of slope-flows, if present, and the interaction of the typical slope-flow dynamics with those of the vegetated RSL dynamics.

To this end, the purpose of the present study is to (i) characterize night-time drainage flow within a vineyard, and (ii) quantitatively and qualitatively describe the turbulent exchanges of heat and momentum during the observed drainage events for a vineyard canopy that is oriented nearly parallel to the terrain slope. It is expected that results presented herein will allow for a more robust understanding of turbulent transport within and above canopies under static atmospheric stability in regions of topographical slopes.

2 Methods

2.1 Site Description and Instrumentation

High-frequency instruments that record airflow, turbulence, and temperature were deployed on a west-facing, 7° vineyard slope in the Burrowing Owl Estate Vineyard in the Black

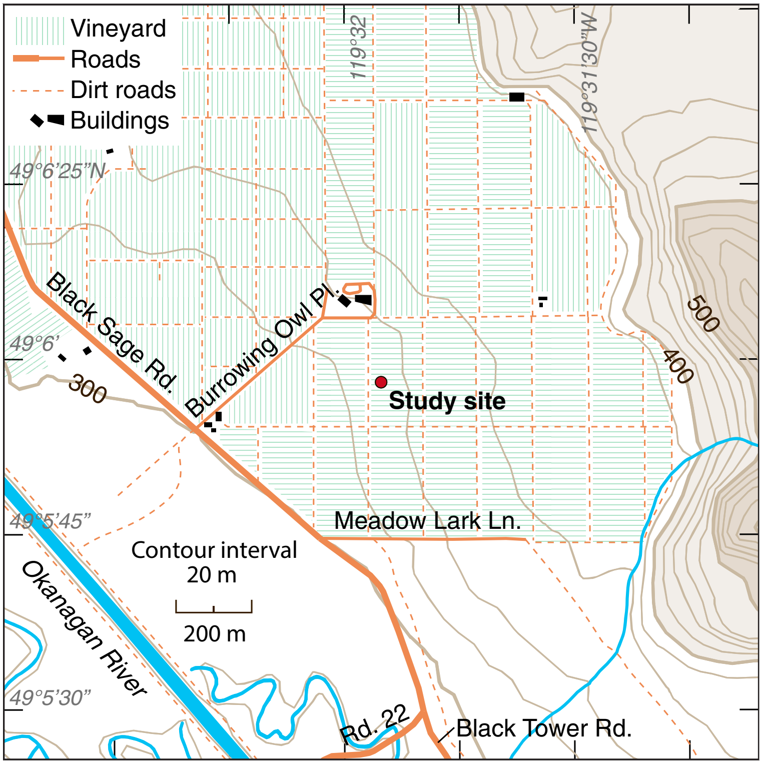

Fig. 1 Topographic map of the study site and surrounding area. Light green lines indicate vineyard crops, and are oriented in the same directions as the crop rows. Orange lines indicate paved (solid) and dirt (dashed) roads. Buildings are indicated by solid black markers. Courtesy of Eric Leinberger

Sage–Osoyoos viticulture region of British Columbia, Canada, between 4 and 22 July 2016. The Black Sage–Osoyoos viticulture region is characterized by sandy, rapidly draining soil with very low moisture holding capacity (Bowen et al. 2005). The site was located 3 km up-valley (north) from the northern tip of Osoyoos Lake, and 1 km downslope (west) of the the foot of steeper mountain terrain. Figure 1 provides a detailed topographic account of the study region. The local terrain slope was measured using an inclinometer to an accuracy of $\pm 1^\circ$; the vineyard canopy height, h_c, was maintained at 2.3 m above ground level (a.g.l.) on average, with the bottom of the leaf area, h_b, located at 0.9 m a.g.l.. Row spacing was maintained at 3 m, and irrigation via a drip-method occurred routinely.

Five ultrasonic anemometers (CSAT3, Campbell Scientific Inc., Logan, Utah, USA) were co-mounted with five Type-E 0.001" fine-wire thermocouples (OMEGA Engineering, Laval, Quebec, Canada) on a 5-m tall pump up mast (Fig. 2) at vertical heights of 0.45, 0.9, 1.49, 2.34, and 4.73 m a.g.l.. Seven 5-m tall masts were installed upslope (east) of the ultrasonic mast at distances of 0.5, 1.0, 2.0, 4.0, 8.0, 16.0, and 32.0 m, on which five fine-wire thermocouples were mounted on each at heights of 0.45, 0.9, 1.49, 2.34, and 4.73 m a.g.l.. Three infrared thermal sensors (IRT, Apogee Instruments Inc., Logan, Utah, USA) were mounted on the ultrasonic mast, one directed at the ground surface below the ultrasonic array ($\mathrm{IRT_G}$), one at the centre of the vineyard vegetation to the north of the tower ($\mathrm{IRT_N}$), and one at the centre of the vineyard vegetation to the south of the tower ($\mathrm{IRT_S}$). All CSAT3 anemometers, fine-wire

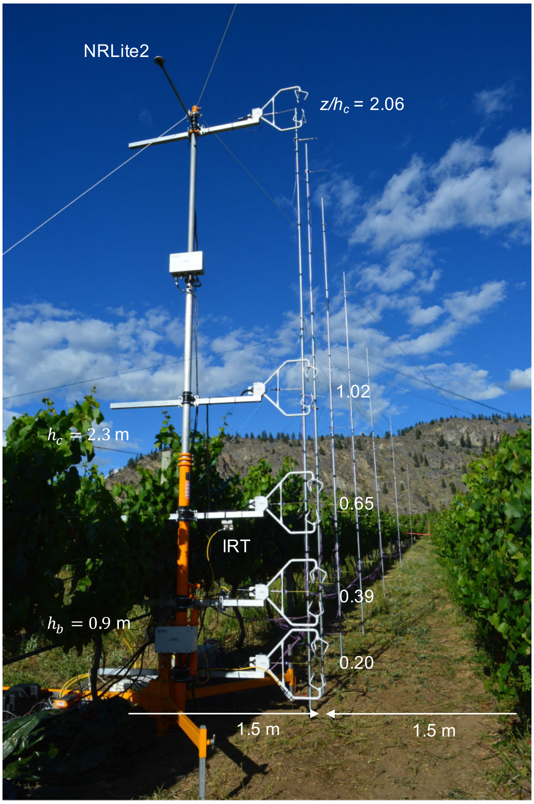

Fig. 2 Photo of the ultrasonic anemometer tower and fine-wire thermocouple mast set-up. Heights are given in m a.g.l., the infrared thermal sensor facing the ground surface is labelled, and the NRLite2, measuring net radiation, is labelled

thermocouples, and infrared thermal sensors were logged by a Campbell Scientific CR3000 data logger. CSAT3s were sampled at 60 Hz, with every three records averaged for a 20-Hz data recording; fine-wire thermocouples and infrared thermal sensors were sampled at 2 Hz. An NRLite2 net radiometer (Campbell Scientific Inc., Logan, Utah, USA) was mounted facing west at 4.8 m a.g.l. on the pump-up tower; samples were logged by and stored at 1-min averaged values on a Campbell Scientific CR1000 data logger. Six extension-grade type-E thermocouples were placed in a vertical array in the soil spaced at 10 mm each to a depth of 60 mm below the soil surface. The soil thermocouple array was located near the centre of the adjacent row to the north of the ultrasonic mast, and was sampled and logged at 1-min intervals by the CR1000 data logger. Volumetric soil water content was sampled once a day at the ultrasonic mast location and at the fine-wire thermocouple mast 32 m upslope using a HydroSense Soil Water Measurement sensor (Campbell Scientific Inc., Logan, Utah, USA).

2.2 Data Post-processing

A two-step rotation was applied to the 3D velocity data as measured by the ultrasonic anemometers. First, the coordinate system was rotated around the z-axis so that the measured x-component at all anemometer heights was aligned with the 5-min mean wind direction at $z/h_c = 2.06$ ($\overline{WD}_{2.06}$). Second, the coordinate system was rotated around the y-axis by an angle equivalent to $\alpha \sin(\overline{WD}_{2.06})$, where $\alpha = 7°$ is the local terrain slope in the vineparallel direction. This rotation scheme sets the x-component to be that along the 5-min mean wind direction and parallel to the local east–west slope, and the z-component to be normal to the local east–west sloping surface, such that all velocity data are projected into a common, terrain-aligned, Cartesian coordinate system. Francone et al. (2012) employ a similar rotation scheme as the one used here. See Everard (2017) for a more thorough analysis regarding our use of the double-rotation tilt-correction method at this site. Linear corrections to the anemometer acoustic temperatures were applied using the temperature measured by the co-located fine-wire thermocouples. This correction does not take into account atmospheric humidity, which is not measured during the campaign. Following Emmel (2014), uncertainties in the TKE (e), mean and turbulent velocity components ($\overline{u_i}$ and u_i', respectively), skewness, and turbulent correlations (i.e., the turbulent fluxes presented herein) were calculated from reported standard deviations from an inter-comparison study that included one of our deployed CSAT3 instruments (Liss et al. 2009). Furthermore, zero-offsets were determined for each CSAT3 by checking the ability of each sensor to measure a zero velocity component in all three component directions when enclosed in a box (no air movement) within a temperature-controlled environment (between 15 and 20 °C). Various rotations of the box were considered, revealing no dependence on orientation, and thus to slight temperature gradients, for any of the CSAT3 instruments. The resulting zero-offsets were applied to the data.

2.3 Case-Study Selection

Nocturnal periods, defined as between 2100 and 0500 local time (LT = UTC − 7 h), were isolated from the full dataset. Five nights were excluded from analysis due to strong synoptic forcing and/or nocturnal thunderstorms. Initial inspection of the gradient Richardson number (R_i, defined in Sect. 2.4.2), wind direction, squared buoyancy frequency (N^2, defined in Sect. 2.4.2), and e at both h_c and the top of the measurement domain, as well as local vertical thermal stratification, revealed two dominant regimes. The first is the anticipated drainage flow regime due to temperature stratification over the local sloping terrain; the second is presumably a stronger valley-flow regime. Under both regimes, net radiation (Q^*) < -30 W m^{-2} and $N^2 > 0$ suggest a statically stable environment. However, strong local vertical stratification is achieved only during the drainage-flow cases, while the valley-flow cases were associated with much stronger forced convection (i.e., $-\frac{1}{3} < R_i < \frac{1}{3}$) and higher TKE, e, compared with the drainage-flow cases.

Using this knowledge, a k-means clustering routine (Wilks 2011) was performed (with number of clusters, $k = 2$) using the 5-min block averaged e and R_i at $z/h_c = 2.05$ and $z/h_c = 1.01$. Prior to clustering, night-time cases with $Q^* < -30$ W m^{-2} were selected, leaving a total of 639 5-min block averages to be evaluated. Following the clustering routine, 17 5-min blocks were reclassified from drainage flow to valley flow because $\overline{WD}$ at $z/h_c = 1.01$ was outside of the downslope domain ($45° < WD_{z/h_c=1.01} < 135°$). Additionally, 81 5-min blocks were reclassified from valley flow to drainage flow because $\overline{WD}$ at $z/h_c = 1.01$ was within the downslope domain and block averaged bulk temperature gradients (between $z/h_c = 0.2$ and $z/h_c = 2.05$) > 1 K m^{-1}. The redistribution step adds pertinent static stability and directional information to the classification clusters. Drainage-flow conditions were found to occur during 25 h of the campaign ($\approx$17.5% of all night-time data).

2.4 Data Analysis Techniques

2.4.1 Averaging Procedures

The 5-min average of a variable, a, is denoted by $\overline{a}$, and the ensemble average of all 5-min temporal averages is denoted by $\langle\overline{a}\rangle$. A 5-min averaging period is chosen to avoid including lower frequency motions in the analysis, and is used in other RSL studies under stable conditions (e.g., Dupont and Patton 2012). While a multiresolution decomposition (Vickers and Mahrt 2006) suggests that a 5-min averaging time is the most consistently appropriate considering both heat and momentum fluxes, due to the static stability during the case studies investigated herein, there is the possibility that results obtained above h_c using the 5-min time-averaging block are biased by internal gravity waves (Pan and Patton 2017) with frequencies lower than N and higher than $\frac{1}{300}$ Hz. Ensemble averages here represent the average of all drainage flow 5-min averaged time blocks, unless otherwise stated. Only drainage flow cases are investigated in the present study. Along-slope spatial ensemble averages of the 5-min mean, which can be calculated for temperatures measured on different masts of the fine-wire thermocouple array at a given height a.g.l., are denoted with curly brackets, $\{\overline{a}\}$.

2.4.2 Stability

The potential temperature is defined relative to the ground, without the slope taken into account. The squared Brunt–Väisälä frequency was calculated using the fine-wire thermocouple array as

$$N^2 = \frac{g}{\theta_{A5}} \frac{\theta_{H5} - \theta_{A5}}{d \, \sin(\alpha)} \tag{1}$$

where g is the acceleration due to gravity, θ_{A5} and θ_{H5} are the potential temperatures at $z/h_c = 2.06$ for the masts located at x-locations of zero (flux tower) and 32 m, respectively, $d = 32$ m is the along-slope distance between θ_{A5} and θ_{H5}, and $\alpha = 7°$ is the slope angle.

The gradient Richardson number, R_i, at $z/h_c = 2.06$ and 1.01 is calculated as

$$R_i = \frac{\frac{g}{T}\frac{\Delta\theta}{\Delta z}}{(\frac{\Delta u}{\Delta z})^2 + (\frac{\Delta v}{\Delta z})^2} \tag{2}$$

where the reference temperature, T, is the corrected temperature measured by the anemometer at $z/h_c = 2.06$, and θ is the potential temperature and has been calculated relative to height a.g.l. using corrected anemometer temperatures. The vertical gradients in velocity components and temperature were determined using spline-fit interpolations.

2.4.3 Conditional Sampling

An octant analysis was applied using the streamwise and the slope-normal velocity deviations, u' and w', respectively, and the potential temperature deviations, θ', from their respective 5-min means. The octant analysis is an extension of the traditional quadrant analysis, whereby temperature information is included in the characterization of the transporting eddies (e.g., Volino and Simon 1994). Momentum sweeps are further divided into warm (O4) and cold (O8) sweeps, ejections into warm (O2) and cold (O6) ejections, inward interactions into warm (O3) and cold (O7) inward interactions, and outward interactions into warm (O1) and cold (O5) outward interactions. Sweeps and ejections are typically associated with coherent,

Table 1 Octants necessary for the calculation of quadrant stress fractions for common quadrant analysis for both the streamwise slope-normal momentum flux ($\overline{u'w'}$) and the slope-normal kinematic heat flux ($\overline{w'\theta'}$)

Description	$\overline{u'w'}$	$\overline{w'\theta'}$
Quadrant 1 (outward interaction)	O1 and O5	O1 and O2
Quadrant 2 (ejection)	O2 and O6	O5 and O6
Quadrant 3 (inward interaction)	O3 and O7	O7 and O8
Quadrant 4 (sweep)	O4 and O8	O3 and O4

or organized, motion within canopies (e.g., Finnigan 2000), whereas motions within the interaction quadrants can be considered 'unorganized' motion, or not likely associated with transport due to large mixing-layer type instabilities near h_c. Summation of the fluxes in relevant octants simplifies the octant analysis to a quadrant analysis for both the streamwise momentum flux and the turbulent sensible heat flux (see Table 1).

A hyperbolic hole is used to not only investigate the importance of shorter-lived, larger magnitude events to the bulk transfer of momentum and heat (e.g., Shaw et al. 1983), but to also constrain the analysis to those events that are not associated with the uncertainty in the slope-angle measurement. The size of the hole, H is defined as

$$H = \frac{|a'w'|}{|\overline{a'w'}|} \tag{3}$$

where the point (a',w') lies on the hyperbola bounding the hole region, and a' represents either u' or v'. The hole size necessary to avoid most of the error related to slope-angle uncertainties is on average $H = 3$ for both stresses.

Stress fractions, $S_{i,H}$, for both the quadrants and the octants, are defined as

$$S_{i,H} = \frac{\sum_{n=1}^{n=N} a'w'_{i,H}(n)}{\sum_{n=1}^{n=N} a'w'_{H}(n)} \tag{4}$$

where $N = 6000$ is the number of samples in the 5-min blocks, a' is either u', v', or θ', i is the octant (or quadrant), H is the hole size—unless otherwise stated, $H = 3$, and $a'w'_{i,H}$ is an instantaneous vertical flux that is greater than or equal to hole-size cut-off flux.

2.4.4 Exchange Efficiency

As a measure of the efficiency of momentum transport along the mean gradient, the exuberance, e_x, of the flow is calculated, which is the ratio of the counter-gradient to along-gradient stresses (Shaw et al. 1983),

$$e_x = \frac{S_{1,H} + S_{3,H}}{S_{2,H} + S_{4,H}} \tag{5}$$

where $S_{2,H}$ and $S_{4,H}$ are the ejections and sweeps characteristic of coherent/organized transport and $S_{1,H}$ and $S_{3,H}$ are the outward and inward interactions characteristic of unorganized transport. If, for example, the action of turbulence was to exactly transport fluid properties along their respective mean gradients, then $S_{1,H} + S_{3,H} = 0$, and $e_x = 0$. If, however, turbulent transport was exactly in opposition to the same mean gradients, then $S_{2,H} + S_{4,H} = 0$ and $e_x = \infty$. Further, it is relevant to note that when $e_x = -1$, the transport of high momentum fluid downwards is equally balanced by the transport of high momentum upwards, and the total flux would be zero. For $-1 < e_x < 0$, transport of high momentum fluid downwards dominates.

2.4.5 Measurements of Sweep/Ejection Cycle Imbalance

Skewness in the velocity components, Sk_u, Sk_v, and Sk_w, and acoustic temperatures, Sk_T, in addition to the ratio between the total contribution of sweeps and ejections to the total flux, are used to characterize the imbalance in transport mechanisms. The imbalance in the sweep/ejection cycle has been investigated both using the ratio of sweeps to ejections (Shaw et al. 1983), and the ratio of ejections to sweeps (Miller et al. 2017). Here, we use the ratio between ejections and sweeps to directly compare results with Miller et al. (2017), viz.,

$$\Delta S_0 = \frac{S_{2,H}}{S_{4,H}}. \tag{6}$$

2.4.6 Turbulence Scales

The two-point length scale ($\ddot{L}$) and one-point time scale ($\dot{T}$) for temperature that are characteristic of turbulence are calculated using the normalized Eulerian correlation tensor, given by

$$\boldsymbol{R}_a(\tilde{x}, \tilde{z}, t, r, d, \tau) = \frac{\overline{a'(\tilde{x}, t)a'(\tilde{x} + r, \tilde{z} + d, t + \tau)}}{(\overline{a'^2(\tilde{x}, \tilde{z}, t)}\ \overline{a'^2(\tilde{x} + r, \tilde{z} + d, t + \tau)})^{1/2}}. \tag{7}$$

Here, $(\tilde{x}, \tilde{z})$ is the stationary sensor origin, t is the time origin, r is the vertical distance and d is the horizontal distance between the stationary and 'roving' sensors, τ is the time lag, and the tilde is used to denote an un-rotated coordinate system.

When possible, an integral scale is often a preferred quantity for characterizing the larger turbulence scales. However, given that the distance-lagged autocorrelations did not often reach zero, estimation of a reliable integral scale was not possible with current approximation methods, thus, we opted to use the length or time at which the correlation fell to $1/\mathrm{e}$ (e.g., Bewley et al. 2012; Tritton 2012).

To calculate time scales, we set $r = 0$ and $d = 0$, and the autocorrelation curves for each sensor are fit with an exponential decay function (e.g., Bewley et al. 2012). The time scale is taken as the value, τ, at which $\boldsymbol{R}_a(\widetilde{x}, \widetilde{z}, t, 0, 0, \tau) = 1/\mathrm{e}$. To calculate length scales, we set $\tau = 0$ and $r = 0$, and fit the slope-parallel distance-lagged correlation curves with an exponential decay function. The two-point distance scale is taken as the separation distance, d, at which $\boldsymbol{R}_a(\widetilde{x}, \widetilde{z}, t, d, 0, 0) = 1/\mathrm{e}$. An average convection velocity is calculated by

$$\overline{uc} = \frac{\ddot{L}}{\dot{T}}. \tag{8}$$

2.4.7 Ground Heat Flux

We calculate the ground heat flux using the soil thermocouple array in the adjacent vineyard row as

$$G = -k\frac{\mathrm{d}T}{\mathrm{d}z} \tag{9}$$

where $k = 0.68\ \mathrm{W\ K^{-1}\ m^{-1}}$ is the approximate thermal conductivity for a sandy soil with a volumetric soil water content of 6%.

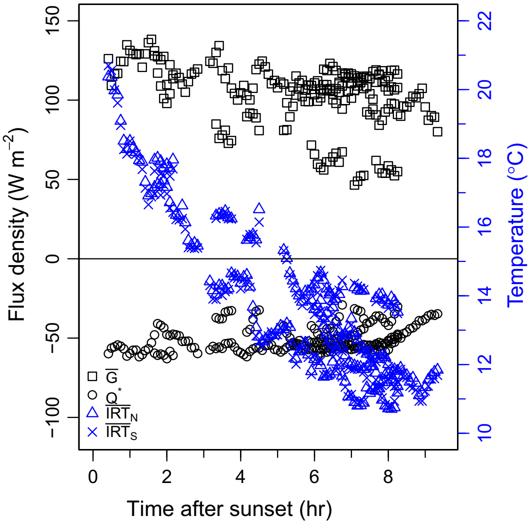

Fig. 3 5-min averaged calculated ground heat flux (black squares), measured net radiation (black circles), measured vineyard surface temperature for northern row (blue triangles), and measured vineyard surface temperature for southern row (blue crosses) as a function of time after sunset (sunset is approximately 2105 LT) for all 211 drainage flow cases considered. The left-hand axis corresponds to the 5-min averaged ground heat fluxes and net radiation, and the right-hand (blue) axis corresponds to the 5-min averaged infrared temperature

3 Results

Figure 3 provides the night-time evolution of two components of the energy balance (black), G and Q^*, and the surface temperature of the vineyard rows (blue) to the north (IRT_N) and south (IRT_S) of the ultrasonic tower for all selected night-time drainage flow cases. The surface acts as an input of heat into the RSL, whereas the net radiative loss at the top of the measurement domain indicates a loss of heat. The canopy elements cool rapidly after sunset, and continue to cool throughout the night.

A temperature inversion is observed within and above the ‘crown space’ of the canopy (i.e., between h_b and h_c), whereas a lapse is present in the near-surface region below h_b (Fig. 4a). The average bulk temperature gradient is 0.73 K m^{-1} between $z/h_c = 0.39$ and $z/h_c = 2.06$, 0.06 K m^{-1} between $z/h_c = 0$ and $z/h_c = 2.06$, and -2.77 K m^{-1} between $z/h_c = 0$ and $z/h_c = 0.39$.

Wind speed increases with height, with an apparent weak inflection point near the canopy top (Fig. 4b), and a jet maximum between $z/h_c = 1.02$ and $z/h_c = 2.34$ (based upon linear interpolation to the zero-crossing in Fig. 5a, as suggested by Grachev et al. 2016). The steepest observed vertical gradients in wind speed are on average between $z/h_c = 0.19$ and 0.39, and between $z/h_c = 0.65$ and h_c. There is no significant gradient in wind speed observed between $z/h_c = 0.39$ and 0.65. The TKE, e, is lowest within the canopy and close to the surface, with the greatest vertical gradient in e between $z/h_c = 0.65$ and h_c (Fig. 4c).

The streamwise momentum flux ($\overline{u'w'}$) is greater in magnitude than that of the cross-stream momentum flux ($\overline{v'w'}$), except for near the ground where both fluxes are within the uncertainty range for the ultrasonic anemometers (Fig. 5a, b). The greatest magnitude in streamwise momentum flux is observed at $z/h_c = 1.01$. The change in sign of $\langle\overline{u'w'}\rangle$ is linearly interpolated to $z/h_c = 1.65$, or $\approx$3.79 m a.g.l. (marked by asterisk, Fig. 5a), suggesting the presence of a jet maximum near this location (e.g., Grachev et al. 2016). Sensible heat flux within the inter-quartile range of the 5-min averaged data is everywhere negative (towards the surface), with the most negative (strongest) flux at the top of the canopy (Fig. 5c).

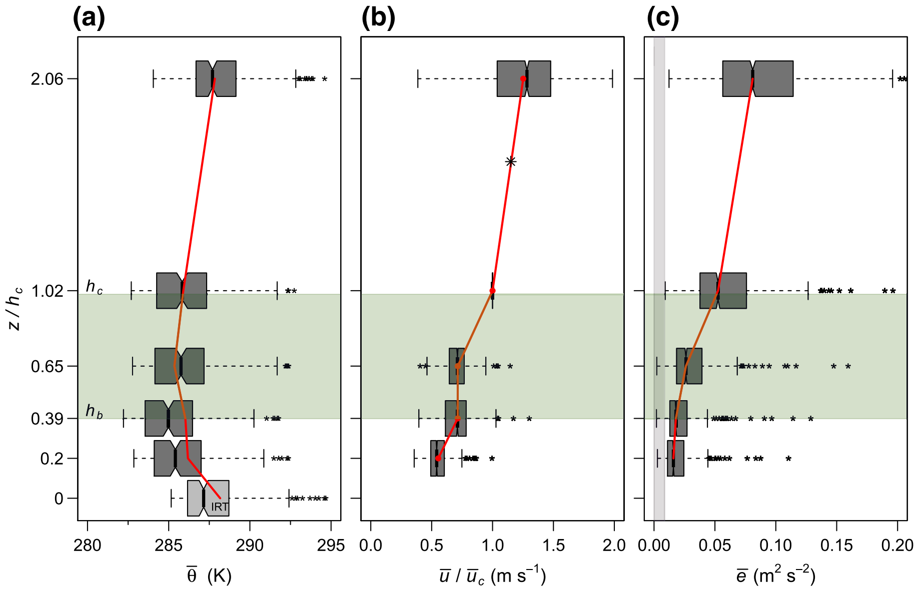

Fig. 4 Box plots of the 211 5-min averaged **a** potential temperature (θ), **b** wind speed (U) normalized by the wind speed at the canopy top (U_c), and **c** turbulence kinetic energy (TKE, e). The interquartile range is represented by shaded boxes, the median is given by the centre-line of the boxes, and outliers are represented by small asterisks. Potential temperature profiles provide air temperatures as measured by fine-wire thermocouples (dark-grey) and soil surface temperatures as measured by the infrared thermal sensors (light-grey). Translucent green shading provides approximate location of the vegetated portion of the vineyard canopy at the site; h_c denotes the approximate top of the canopy; h_b denotes the approximate bottom of the vegetated portion of the vineyard canopy. Light-grey shading represents the uncertainty in the calculated TKE. Ensemble average for all quantities is given by red line. The large asterisk in (**b**) indicates the location of the interpolated jet maximum

Within the canopy, skewness in the streamwise velocity component (Sk_u) is positive, except for at the top of the ultrasonic array where average Sk_u is within the instrument uncertainty range (Fig. 6a). Skewness in the spanwise velocity component (Sk_v) is very small and within the uncertainty bounds at the top three heights ($z/h_c = 2.06, 1.02,$ and 0.65), and is negative near the ground surface (Fig. 6b). Skewness in the slope-normal velocity component (Sk_w) is near zero near at the top of the measurement domain, positive at the canopy top, and then negative within the canopy (Fig. 6c). Skewness in the corrected acoustic temperature (Sk_T) is positive within the canopy and negative at the top of the measurement domain (Fig. 6d).

Figure 7a provides the ensemble-averaged streamwise momentum flux quadrant fractions. Coherent, or organized, transport is represented by a positive flux fraction, whereas unorganized transport is represented by a negative flux fraction. Indicative of the presence of a jet maximum, the contribution of the different quadrants to the total stress changes sign between h_c and the top of the measurement domain. Within the canopy, quadrants 2 and 4 contribute the most to the streamwise momentum flux, with quadrant 4, which is associated with sweeps, dominating at and below $z/h_c = 0.65$ (Fig. 7a).

Figure 7b provides the exuberance, e_x, as a function of height. We adopt a flexible definition of e_x so that it represents the efficiency of the transport of high momentum fluid downwards below the jet peak, and high momentum fluid upwards above the jet peak. When $e_x = -1$, the

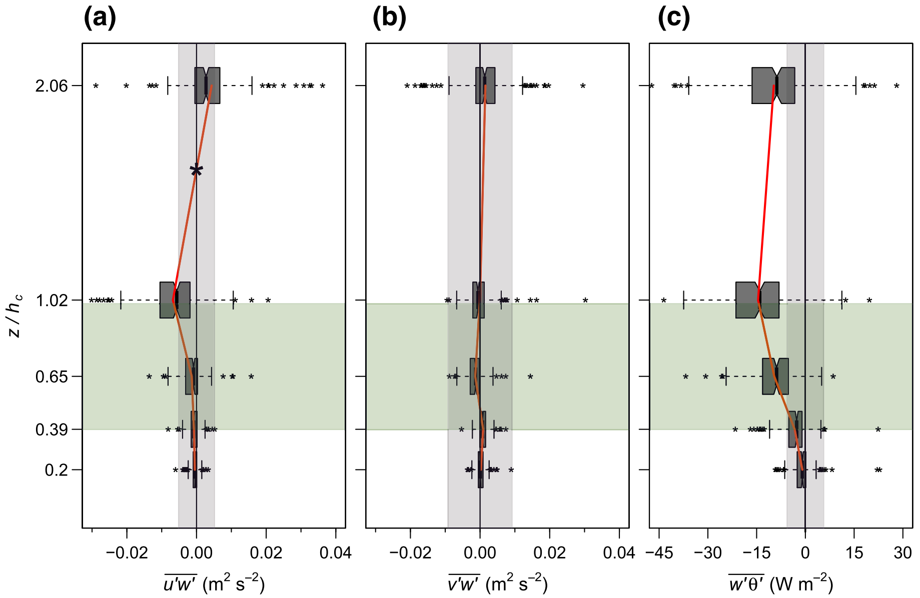

Fig. 5 Box plots of the 211 5-min averaged, **a** streamwise vertical momentum flux, **b** cross-stream vertical momentum flux, and **c** kinematic vertical sensible heat flux. Asterisk at $z/h_c = 1.65$ in **a** gives the location of the interpolated jet-height. Ensemble average for all quantities is given by red line. Green shading is defined in Fig. 4. Light-grey shading represents the measurement uncertainty for the calculated fluxes

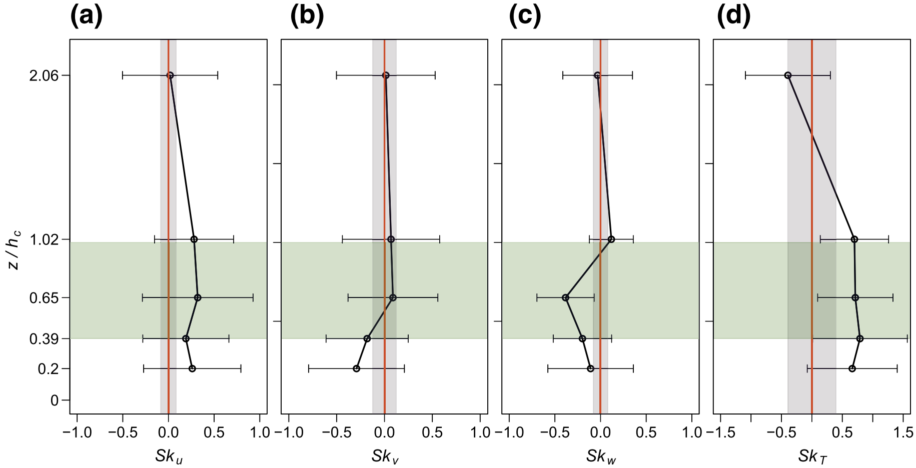

Fig. 6 Vertical profiles of ensemble-averaged skewness in the 5-min drainage flow cases for, **a** streamwise velocity, Sk_u; **b** cross-stream velocity, Sk_v; **c** vertical velocity, Sk_w; and **d** acoustic temperature, Sk_T. Error bars represent the standard deviation in the ensemble average of all 211 drainage flow cases, and the light-grey shading represents the measurement uncertainty. Green shading is defined in Fig. 4

transfer of high momentum fluid downwards below the jet peak (upwards above the jet peak) is equal to the transfer of low momentum fluid downwards (upwards). When $-1 < e_x < 0$, the transport of high momentum fluid downwards (upwards) exceeds that of the transport of low momentum fluid downwards (upwards). While everywhere in the domain exchange

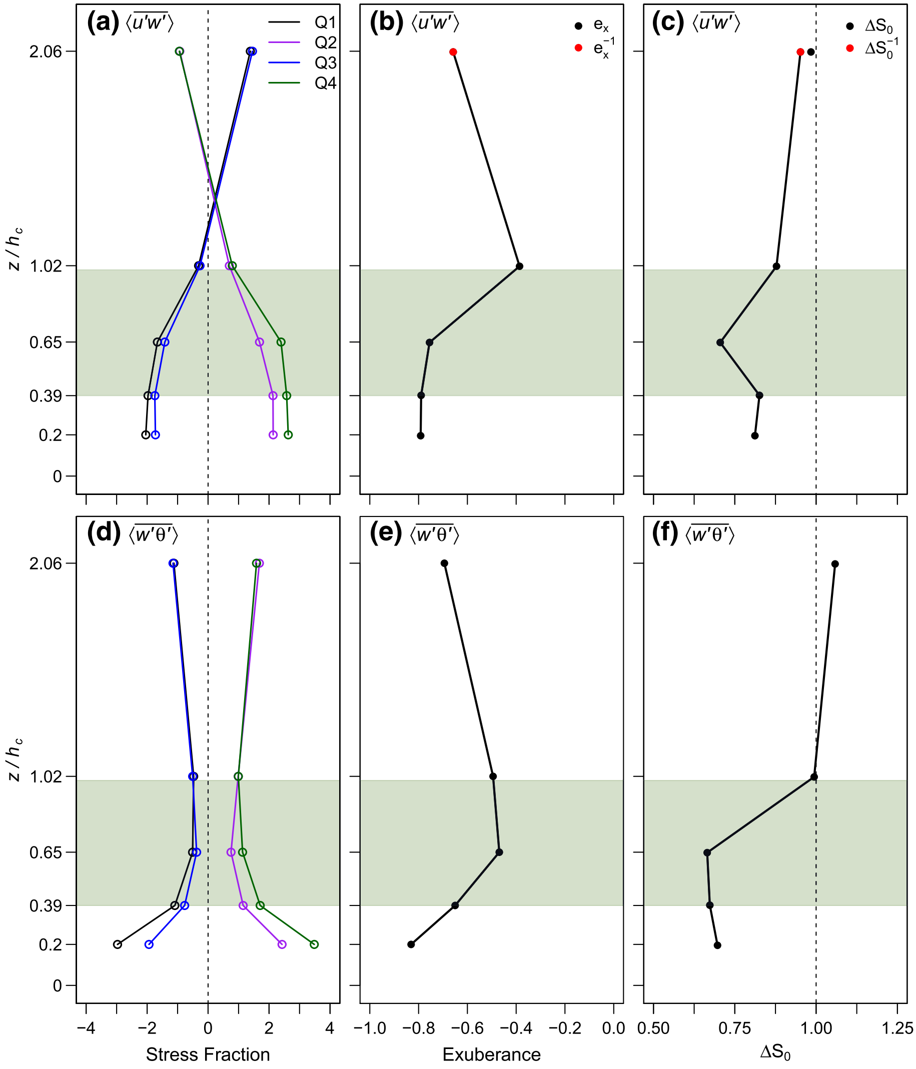

Fig. 7 Ensemble-averaged, **a** quadrant stress fractions for $\overline{u'w'}$, **b** exuberance of $\overline{u'w'}$, **c** ejection-to-sweep ratio (ΔS_0) for $\overline{u'w'}$, **d** quadrant stress fractions for $\overline{w'\theta'}$, **e** exuberance of $\overline{w'\theta'}$, and **f** ΔS_0 for $\overline{w'\theta'}$. A hole size of $H = 3$ was used for the quadrant stress fractions for $\overline{u'w'}$, and a hole size of $H = 0$ was used for $\overline{w'\theta'}$. Green shading is defined in Fig. 4

of streamwise momentum is efficient (i.e., associated with coherent motion and $-1 < e_x$), exchange is most efficient at the canopy top (Fig. 7b).

Figure 7c provides the ratio of the stress fractions in momentum ejections to that of momentum sweeps as a function of height. Sweeps are most dominant near the centre of the crown space ($z/h_c = 0.65$), and remain dominant, although to a lesser extent, within and above the canopy (Fig. 7c). Figure 7d–f are the same as Fig. 7a–c, except for the turbulent sensible heat flux. Quadrants 2 and 4 contribute to the turbulent sensible heat flux along the gradient characterized by the bulk temperature inversion over the full measurement layer (Fig. 7e). Within

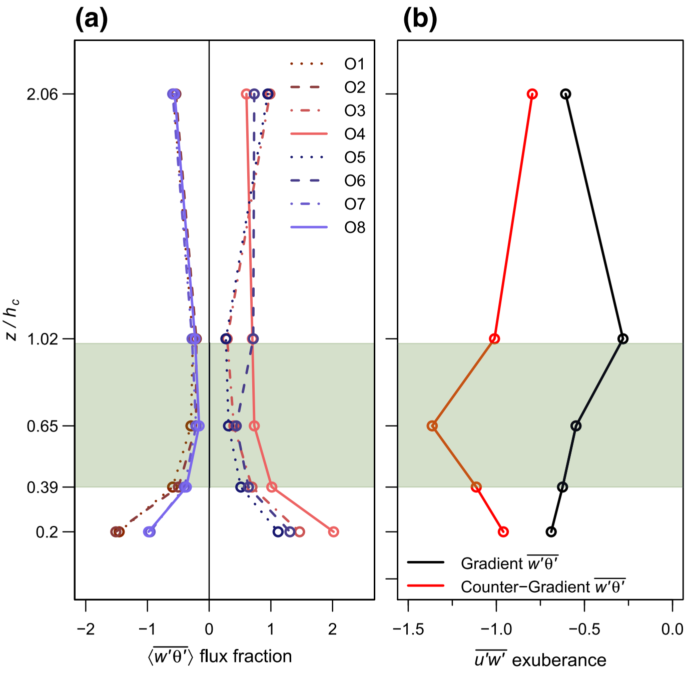

Fig. 8 **a** Octant heat flux fractions. Blue colours are associated with $-\theta'$ and red colours with $+\theta'$. Solid lines represent organized transport of streamwise momentum, and dashed lines represent unorganized transport of streamwise momentum. **b** Separation of the streamwise momentum flux exuberance into instances of gradient (along a general temperature inversion; red) and counter-gradient (against a general temperature inversion; black) kinematic sensible heat flux. Green shading is defined in Fig. 4

the canopy, quadrant 4, which is associated with sweeps, contributes the most to the transport of heat. The flow is most exuberant within the top portion of the canopy (between $z/h_c = 0.65$ and 1.02; Fig. 7e). At the canopy top, the ejection/sweep ratio is close to 1 (Fig. 7d). Sweeps dominate within the canopy, particularly closer to the ground, whereas at the canopy top and above the jet, ejections become more important to turbulent sensible heat transport (Fig. 7f).

Figure 8a provides the ensemble-averaged flux fraction in each octant for the heat flux as a function of height. The colouring corresponds to whether the octant represents a negative temperature deviation (blue) or a positive temperature deviation (red) relative to the 5-min block average. The solid lines correspond with the octants representing organized (or coherent) streamwise momentum transport, whereas the dashed or dotted lines correspond with the octants representing unorganized transport of streamwise momentum. Octants 3, 4, 5, and 6 represent organized transport of heat (warmer air downwards and colder air upwards), and octants 1, 2, 7, and 8 represent unorganized transport of heat. At all heights, the total turbulent heat flux is along an inverted temperature gradient (Fig. 8a). Octants 4 and 6 contribute the most to the flux fraction, which are associated with coherent streamwise momentum transport. Further, octant 4, which is associated with sweeps of high momentum and higher temperature, contributes the most to the heat flux within the canopy (Fig. 8a).

Figure 8b provides a breakdown of the streamwise momentum-flux exuberance as a function of heat transport either along the bulk temperature inversion (black) or against the inversion (red). When $\langle\overline{w'\theta'}\rangle$ is negative (along inversion), momentum transport is exuber-

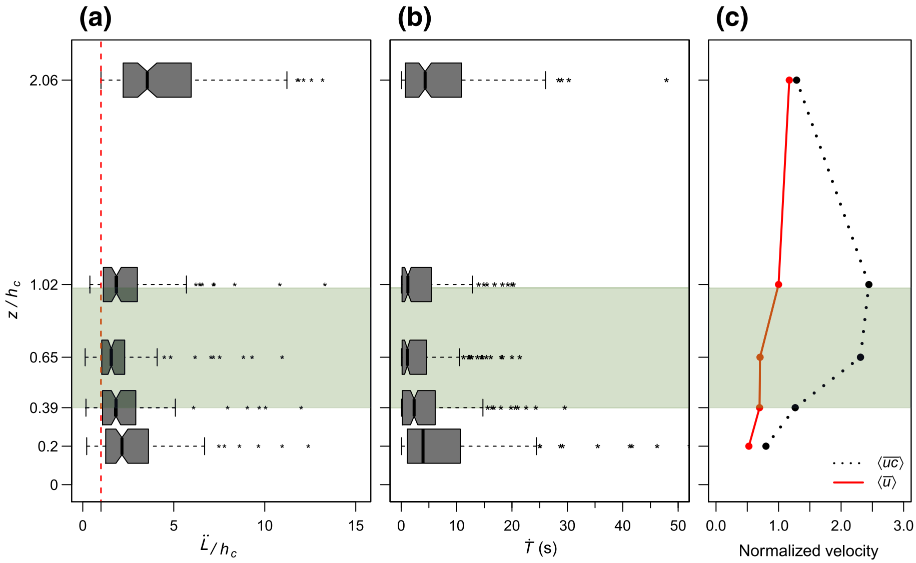

Fig. 9 Box-plots of, **a** two-point (slope-parallel) length scale ($\ddot{L}$) normalized by canopy height, **b** unnormalized single-point time scales ($\dot{T}$) for the 211 5-min drainage flow cases, and **c** ensemble-averaged vertical profiles of convection velocity ($\overline{uc}$) and streamwise velocity component ($\overline{u}$) normalized by the streamwise velocity component at h_c (u_c). Green shading is defined in Fig. 4

ant, i.e., more coherent (Fig. 7b). When $\langle \overline{w'\theta'} \rangle$ is positive (against inversion), the transport of streamwise momentum is not exuberant, indicating that neither sweeps nor ejections dominate the transport of sensible heat against the temperature inversion (Fig. 8b). In particular, inward and outward interactions, which are not associated with coherent motions, become more important to the counter-inversion transport of sensible heat near the centre of the canopy, whereas near the canopy top and the surface, there is no discernible preference towards organized or unorganized momentum transport and the counter-inversion transport of sensible heat (Fig. 8b).

Figure 9 provides the two-point length scale ($\ddot{L}$; Fig. 9a), one-point time scale ($\dot{T}$; Fig. 9b), and ensemble-averaged convection velocities normalized by the velocity at h_c ($\langle \overline{uc/u_c} \rangle$, Fig. 9c). The scale $\dot{T}$ is shortest within the canopy, with the longest $\dot{T}$ occurring at the top of the measurement array (Fig. 9b). The scale $\ddot{L}$ follows the time scale pattern closely; $\ddot{L}$ scales well with h_c within the canopy, particularly near the centre of the canopy (Fig. 9a). The behaviour of $\ddot{L}$ and $\dot{T}$ across the entire domain results in quicker convection velocities at the canopy top and within the canopy, and slower convection velocities at the top of the measurement domain and near the surface (Fig. 9c).

Figure 10 is an ensemble-averaged contour plot of the spatial temperature correlations. Positive distances in the plot indicate a correlation in which the 'stationary' fine-wire thermocouple is downslope (x-direction) of, or vertically (z-direction) below, the 'roving' sensor. As an example, the correlations at upslope distances of -32 m indicate that mast H was defined as 'stationary' and mast A was defined as 'roving'. Therefore, the terms 'stationary' and 'roving' used in this context do not imply the actual movement of the sensors, but the fact that spatial correlations are calculated with each fine-wire thermocouple taken at some point as the spatial origin, which is given by $(x, z) = (0, 0)$ in the plot. This means that the correlation at $(0, 0)$ in Fig. 10 represents the time-ensemble average between the zero-time

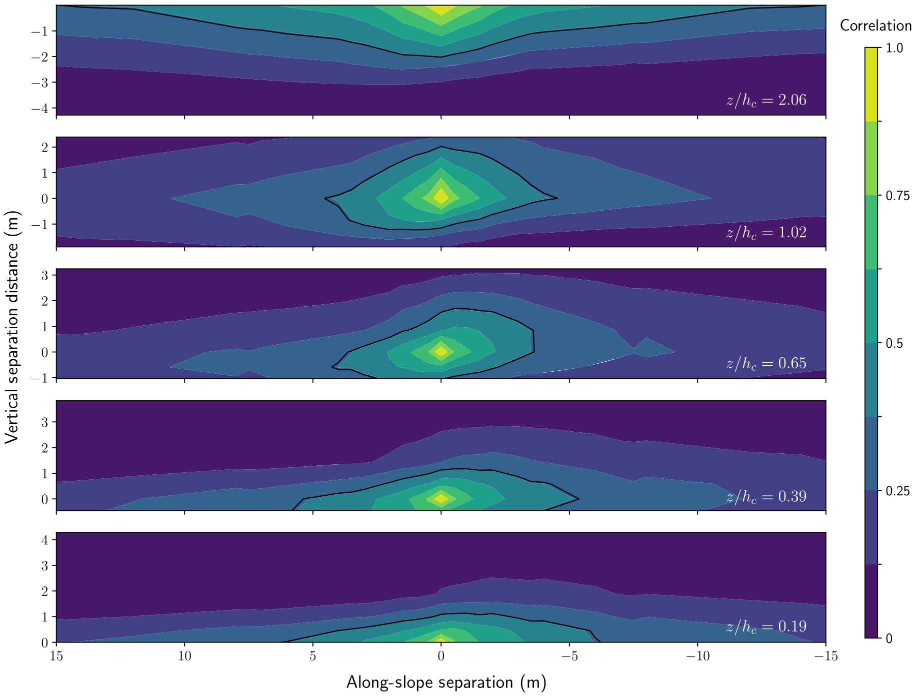

Fig. 10 (Time) ensemble-averaged two-point correlations between all possible fine-wire thermocouple distance combinations. Correlations made upslope are positive x-distances, and correlations made upwards are positive z-distances. The plot is oriented so that to the left of the correlation centre, distances are upslope from the centre, and to the right of the centre correlations are downslope from the centre. Black contour is the e-folding correlation value used for determining two-point length scales

lagged autocorrelations of all 40 fine-wire thermocouples (an average between 8440 total correlations, which is trivial as the zero-time-lagged autocorrelation of one sensor with itself is identically 1.0). Following the ensemble-averaging procedure and prior to contour plotting, all negative correlations are shown as zero correlations. This exaggerates the extent of ‘no correlation’ at the edges of the plotting domains, but allows for intercomparison between the five different heights.

There is agreement between calculated longitudinal length scales and the size of the eddies in Fig. 10, whereby the largest structures are located at the top of the measurement domain and the smaller structures are located within the crown space. According to Fig. 10, eddies are more circular near the top of the canopy, whereas within the canopy space, the structures are flatter, and near the centre of the crown space ($z/h_c = 0.65$), are inclined upwards from the surface facing downslope at an approximate angle of 18°.

4 Discussion

4.1 Mean Characteristics

Contrary to typical drainage flows over bare slopes, we observe an elevated inversion within the drainage layer at the study vineyard site starting around $z/h_c = 0.39$. Such elevated inversions have been observed within the trunk-spaces of denser canopies under stable night-time conditions (e.g., Jacobs et al. 1994; Dupont and Patton 2012). Under similar conditions within open canopies, however, inversions have been observed to start near the ground surface (Launiainen et al. 2007). Given that the vineyard canopy is open (relative to a dense forest), the soil is dry, and that the chosen case studies are characterized by relatively clear skies, the existence of the trunk-space lapse is not fully understood. While the ground heat flux is directed towards the surface (Fig. 3), it is apparent that neither the canopy, nor the near-surface air, warm throughout the night (Fig. 3). This raises questions in regards to where this added heat is transported and/or stored. Ultimately, the presence of the near-surface lapse indicates that the observed drainage flow is not driven by radiative cooling at the surface, but most likely forms due to cooling of the steeper (and essentially bare) terrain to the north-east of the site (Fig. 1), and drains into the region. Given the cooling of the vegetation elements throughout the night (Fig. 3), it is also likely that the canopy plays a role in at least the sustainment of the local night-time drainage layer.

It is clear, given the weak inflection point near h_c (see Fig. 4b) and the interpolated near-surface jet peak within the measurement domain (Fig. 5a), that both dynamics related to drainage and typical RSL flows are present during the selected drainage-flow cases. An inflection in the mean velocity profile implies a region of hydrodynamic instability where larger coherent structures, which are responsible for a large fraction of momentum transfer in canopies, can be generated (e.g., Finnigan 2000; Thomas and Foken 2007a). Not only does the drainage-flow jet act as a near-h_c source of high momentum fluid to feed turbulence within the canopy-space, but the presence of the jet likely increases TKE within the drainage-flow layer (that includes the RSL), particularly near the jet maximum despite stable stratification (Oldroyd et al. 2016). We surmise that the interaction of the drainage dynamics with the canopy acts to increase turbulent exchange within the RSL during statically stable conditions in the vineyard.

4.2 Turbulent Characteristics

4.2.1 Turbulent Exchange

The conjecture regarding the underlying mechanisms behind turbulence generation within the canopy space is supported by the observations. For instance, TKE is greatest near the canopy top, and quickly decays with distance towards the ground (Fig. 4c). Furthermore, not only does the presence of the jet maximum supply the necessary momentum for dynamic, near-h_c, instability during statically stable conditions, but it also affects the behaviour of total turbulent exchange between the surface and the outer environment. While high momentum is transferred efficiently downwards towards the surface below the jet peak, high momentum is also transferred upwards away from the jet and the canopy, albeit less efficiently (Fig. 7b). Interestingly, there is a slight preference towards the transport of cooler air upwards at $z/h_c = 2.06$ ($\frac{Q5+Q6}{Q3+Q4} = 1.06$; Fig. 7f), implying not only that heat exchange within what is typically defined as the RSL is additionally affected by drainage dynamics, but also that heat and momentum transport is similar above the jet peak. This possibly suggests that turbulence becomes decoupled from the surface above the jet peak, which has been found in more classical drainage flows (e.g., Grachev et al. 2016). For the turbulent sensible heat flux, the cross-over from ejection-dominated to sweep-dominated exchange is observed very near $z = h_c$. While it can be expected that the location of sweep-to-ejection dominated cross-over in the RSL for $\langle\overline{w'\theta'}\rangle$ to be lower than that for $\langle\overline{u'w'}\rangle$ in a row-gap oriented urban canopy

(Christen et al. 2007), this cross-over is even lower still. Additionally, given that stability tends to increase the effective canopy height (Miller et al. 2017), the estimated height of cross-over for $\langle \overline{w'\theta'} \rangle$ can be considered an upper bound for what it may truly be. This decrease in the height of cross-over for $\langle \overline{w'\theta'} \rangle$ is likely another artefact of the drainage and its influence over canonical canopy flow dynamics.

The profile of the ejection/sweep ratio for $\langle \overline{u'w'} \rangle$ follows that reported by Shaw et al. (1983) for a corn canopy over flat terrain under near-neutral conditions. Further, both the average observed location of sweep-dominated to ejection-dominated crossover and the general observed vertical profiles of ΔS_0 for $\langle \overline{u'w'} \rangle$ during the drainage-flow cases are comparable with the profiles of ΔS_0 for the row-parallel momentum fluxes reported by Miller et al. (2017) for a trellised vineyard during near-neutral conditions (cross-over occurred around $z/h_c = 2.4$). The near- and within-canopy domination of sweeps to the exchange of momentum (for example, see Figs. 6a, c, d and 7a, c, d, f) is unsurprising. However, in contrast to what is reported in other studies on airflow in canopies (Dupont and Patton 2012; Miller et al. 2017), the most negative Sk_w, which is associated with sweeping motions, is here found near the centre of the canopy as opposed to near h_c. In fact, at the canopy top, $Sk_w > 0$, which is associated with ejecting motions. This is supported by the ejection/sweep ratios, which for both $\langle \overline{u'w'} \rangle$ and $\langle \overline{w'\theta'} \rangle$, reach a minimum near the centre of the canopy (Fig. 7c, f). Notably, the exuberance rapidly approaches -1 between $z = h_c$ and the canopy top. This is not completely surprising, and could be an indication that the static stability within the canopy environment, coupled with the loss of momentum as the penetrating structures do work against the canopy drag, inhibits deeper penetration of the eddies generated near the canopy top to the surface, and thus the total flux in the near-surface region is less effected by instability near $z = h_c$. The average ΔS_0 for $\langle \overline{u'w'} \rangle \approx 0.8$, whereas for the row-parallel momentum flux in the neutral cases studied by Miller et al. (2017), the average was found to be ≈ 0.7.

The downward turbulent heat flux near the surface, which counters the local gradient, is likely due to a combination of the presence of the drainage layer and vegetated RSL turbulent dynamics. Consistent with other canopies under near-neutral stability (e.g., Finnigan 2000), sweeps and ejections are the most dominant transport processes for sensible heat in the vineyard (Fig. 8a). Further, sweeps dominate within the canopy, with increasing dominance as the surface is approached (Fig. 8a), consistent with behaviour over rough surfaces over flat terrain (Raupach 1981). The fact that sweeps dominate within the canopy and that the canopy is cooling, further validates the assumption that the negative heat fluxes within the canopy (despite the temperature lapse) are not erroneous measurements (Cava et al. 2006). Further, it is apparent that the coherent transport of heat (i.e., along the bulk inversion gradient and associated with sweeps and ejections) is connected to the coherent transport of momentum (Fig. 8b). This could indicate that the structures sweeping into and out of the canopy retain to some extent their ‘original’ temperature (where original here does not necessarily mean an absolute origin). Therefore, it is likely that as higher momentum fluid is swept into the canopy, so too is warmer air. If the penetration of structures is deep enough, this warmer air can reach the near-surface region. Despite the near-surface lapse, the average temperatures are still lower than those above the canopy and even within the canopy (Fig. 4a); thus, similar transport of heat and momentum within the canopy would result in a measured negative turbulent heat flux in the region, meaning only that ejecting motions are slightly more prevalent for the case studies presented here.

4.3 Turbulent Scales and Coherent Structures

Average turbulent length ($\ddot{L}$) and time ($\dot{T}$) scales are smallest near the canopy top (Fig. 9), which is in agreement with the apparent inflection point in the average velocity profile and peak in TKE (Fig. 4). The average length and time scales provide insight into the spatio-temporal extent of coherence in the temperature fluctuations. The greater the length scale, the more correlated temperature fluctuations are along the slope at any instance in time (on average), and the greater the time scale, the longer the correlation in temperature fluctuations is observed at a particular fine-wire thermocouple (on average). As is the case in the urban environment, where flow channelling and canopy top shear are also important, $\ddot{L}$ increases towards the surface from h_c, and also increases upwards from h_c (Christen et al. 2007). This is a direct effect of the differences in shear magnitude as a function of height, which is otherwise not well observed in other, unstructured, canopies where turbulent length and time scales remain generally constant throughout the canopy (Finnigan 2000). Near the canopy top, and within the canopy leaf-area, large velocity shear and work against the canopy drag may prevent any one structure from remaining spatio-temporally coherent for long. Below the leaf-area of the canopy, near the surface, the larger observed length and time scales likely have more to do with the decrease in turbulent activity thus reducing the mixing of near-surface air, allowing for greater spatio-temporal coherence of near-surface air temperatures.

It is further apparent that while the smaller eddies move comparatively quicker than the larger eddies, more intense mixing, such as that observed near h_c, results in quicker moving eddies (Fig. 9). The ensemble-averaged convection velocity observed at the top of the vineyard canopy is much larger compared to that observed in the wind-tunnel study of Shaw et al. (1995) (three times the Eulerian velocity as opposed to two times the Eulerian velocity). This difference is likely due to the use of temperature correlations, which are likely more spatially correlated allowing for larger convection velocities, as opposed to the velocity correlations used by Shaw et al. (1995) in their calculations. As a more direct interpretation of the spatio-temporal scales, the along-slope spatial coherence of temperature is much shorter lived within the canopy, particularly near the canopy top, compared to that in the above-canopy and above-jet-peak region (Fig. 9c). A range of eddy sizes are produced in this high-shear region, with the smaller eddies remaining within the eddy-production zone and quickly decaying, and the larger eddies traveling (mostly) downwards into the canopy and decaying therein.

Structures at the centre of the canopy are inclined at an angle of approximately 18° to the sloped surface, as would be expected for the dual ejection/sweep hairpins generated near canopy top (e.g., Shaw et al. 1995; Finnigan et al. 2009), while those at the top of the domain are not significantly inclined, and are more elongated in the row-parallel direction (Fig. 10). The elongation along the drainage path is a result of the drainage-flow layer and channeling between rows where there is minimal roughness to break up or distort larger structures.

4.4 Uncertainty

While our results advances our understanding of night-time stably-stratified RSL turbulence, results herein are subject to a variety of uncertainties. Over 50% of the turbulence data were obtained under conditions with $u_* < 0.08 \text{ m s}^{-1}$, and most of the measured and calculated components from the ultrasonic anemometers are within the instrument uncertainty limits. Stiperski and Rotach (2016) have shown that strict data quality criteria for flows over complex terrain can result in the elimination of up to 98% of the available data, and Klipp (2018) cautions that over-correction of turbulence data, particularly in the case over complex terrain, can wash out the signals related to real and important physical mechanisms associated with the flow. Thus, it is still necessary to report and explore data such as those presented herein, despite the relatively high uncertainty due to low-wind conditions. It is further recognized that the current anemometry is unable to capture the very small scale turbulent wakes produced by the canopy elements, and that within the canopy, the conversion from lower frequency turbulence to frequencies outside the detection range of the ultrasonic anemometers likely occurs (e.g., Finnigan 2000; Cava and Katul 2008), thus further lending to an underestimation of the total flux. This issue is not unique to the present field study, however, and is a common difficulty faced by all studies relying upon measurements from ultrasonic anemometry.

It is further worth noting that the quadrant analysis employed here tends to underestimate the contributions due to ejections. It is well known that sweeps in the canopy tend to be larger, more infrequent events, whereas ejections tend to be smaller, more frequent events (e.g., Thomas and Foken 2007a). Due to the use of the hyperbolic hole method, we are knowingly excluding a number of smaller ejection events. However, as these fluxes are very small, and do not lend an incredible amount to the total flux, conclusions made regarding total flux contributions are not affected. Further, the quadrant analysis does not represent the spatial or temporal scales of the transporting eddies, making it difficult to conclusively link the transport of heat and momentum with the passing of the coherent structures at the described scales.

Finally, static stability introduces the possibility for the propagation of gravity waves at frequencies lower than the buoyancy frequency, particularly above h_c where the strength of stability is greatest, and the presence of the near-surface lapse raises further questions on the role of gravity waves in nocturnal heat transport (Lee and Barr 1998). While an investigation into the role of gravity waves on the turbulence in drainage flow over organized vegetated canopies is beyond the scope of this paper, there is the possibility that gravity-wave activity has an influence on flow statistics during the night-time drainage flows presented herein, and is worth further consideration in future studies involving this novel dataset.

5 Summary and Conclusions

High-frequency velocity and spatially-distributed, high-frequency temperature measurements were made over and within a vineyard on a 7° slope in order to assess turbulent exchange of heat and momentum under drainage flow conditions. Typical drainage flow at the site is characterized by an elevated inversion, beginning around $z/h_c = 0.39$, and a persistent near-surface lapse. The nature of the surrounding topography in concert with the local near-surface lapse suggests that the drainage flow is initiated by larger scale terrain features to the north and north-east of the site, but is also buoyantly fed by cooling of the vineyard canopy throughout the night. Mean and turbulent features of the observed drainage flow resemble both those for a characteristic drainage layer and for a canopy-plane mixing layer. A weak inflection point is identified in the velocity profile near the top of the canopy, while a near-surface jet peak is estimated around $z/h_c = 1.65$ using linear interpolation between the streamwise momentum flux at $z/h_c = 1.02$ and $z/h_c = 2.06$. The duality of the situation is found to influence RSL exchange of heat and momentum.

Unsurprisingly, the region of greatest TKE in the measurement domain is near the top of the canopy. This region is not only where the typical hydrodynamic instability is located, but also immediately below the interpolated jet peak. Unlike most studies described in the literature, the proximity of the jet to the canopy top adds a further characteristic turbulent transport of heat and momentum away from the near-canopy environment. As observed for near-neutral conditions (e.g., Li and Bou-Zeid 2011), heat and momentum exchange appear to be affected by similar transport mechanisms—specifically, the generation of large coherent structures near canopy top. This co-transport of heat and momentum is likely the reason for the movement of colder air upwards away from the canopy at the top of the measurement domain. As is expected for canopy flow, the transfer of the streamwise momentum is exuberant, with the most efficient transfer occurring at the canopy top. Sweeps dominate everywhere, but are particularly important at the centre of the canopy, likely due to proximity to the top of the canopy where the coherent structures are generated.

Coherent structure visualization via spatial temperature correlations indicate that the structures dominating the transfer of heat are elongated in the streamwise direction. An inclination angle $\approx 18^\circ$ relative to the sloped surface is observed. The ensemble-averaged structures observed in the heat signature of the flow and the inclination angle of the structures gives evidence for the ejection/sweep generating dual hairpin structure that is thought to drive larger scale RSL turbulence (e.g., Finnigan et al. 2009).

Due to the selected measurement set-up, our study is one of the first to investigate in detail the effects of drainage flow on turbulent exchange within the vegetated RSL. Further, the unique set-up of the thermocouple arrays allows for field observations of two-point correlations, which has to our knowledge only been accomplished in wind-tunnel and numerical studies. Knowledge on the turbulent exchange of heat and momentum within agricultural canopies, particularly those potentially affected by thermally-induced circulations, is pertinent to the proper design of agricultural management practices. Observations made during this study suggest that the coldest air is advected in to the agricultural region, and not locally produced, indicating a potential for advective frost risk during times of slope drainage. At the same time, the drainage flow itself seems to enhance vertical mixing which could act as a countermeasure to block or deflect cold air from the steep mountain slopes from ‘settling’ in the vineyard, thus lessening the need for wind machines to instigate vertical mixing for frost damage protection under these drainage flow conditions. Results discussed herein make it apparent that consideration of thermally-induced mountain circulations is important to understanding the turbulent nature of the vegetated RSL during the night-time.

Acknowledgements We would like to thank the owner and staff of the Burrowing Owl Estate Winery for allowing our use of the vineyard during the field campaign. We would also like to thank Paul Skaloud and technical staff at UBC who helped with the logistics of the field campaign, and Drs. Andrew Black, Marco Giometto, Rob Stoll, and Andrew Sturman, who provided valuable insight relevent to this study. Selected equipment was supported by the Canada Foundation for Innovation (Grant #33600, Christen) and NSERC RTI (Christen). Financial support through scholarships and training were provided by UBC Faculty of Graduate and Postdoctoral Studies and UBC Faculty of Arts. This research was partially supported by a Discovery Grant of the National Science and Engineering Research Council of Canada and by the National Science Foundation (NSF-PDM-1848019).

References

Aubinet M (2008) Eddy covariance CO_2 flux measurements in nocturnal conditions: an analysis of the problem. Ecol Appl 18(6):1368–1378

Aubinet M, Heinesch B, Yernaux M (2003) Horizontal and vertical CO_2 advection in a sloping forest. Boundary-Layer Meteorol 108:397–417

Bailey BN, Stoll R (2013) Turbulence in sparse, organized vegetative canopies: a large-eddy simulation study. Boundary-Layer Meteorol 147(3):369–400

Belcher S, Finnigan J, Harman I (2008) Flows through forest canopies in complex terrain. Ecol Appl 18(6):1436–1453

Bewley GP, Chang K, Bodenschatz E (2012) On integral length scales in anisotropic turbulence. Phys Fluids 24(6):061,702. https://doi.org/10.1063/1.4726077

Bowen P, Bogdanoff C, Estergaard B, Marsh S, Usher K, Smith C, Frank G (2005) Geology and wine 10: use of geographic information system technology to assess viticulture performance in the okanagan and Similkameen valleys, British Columbia. Geosci Canada 32(4):161–177

Cava D, Katul GG (2008) Spectral short-circuiting and wake production within the canopy trunk space of an alpine hardwood forest. Boundary-Layer Meteorol 126(3):415–431. https://doi.org/10.1007/s10546-007-9246-x

Cava D, Katul GG, Scrimieri A, Poggi D, Cescatti A, Giostra U (2006) Buoyancy and the sensible heat flux budget within dense canopies. Boundary-Layer Meteorol 118(1):217–240. https://doi.org/10.1007/s10546-005-4736-1

Chahine A, Dupont S, Sinfort C, Brunet Y (2014) Wind-flow dynamics over a vineyard. Boundary-Layer Meteorol 151:557–577. https://doi.org/10.1007/s10546-013-9900-4

Chen H, Yi C (2012) Notes and correspondence: optimal control of katabatic flows within canopies. Q J R Meteorol Soc 138:1676–1680

Christen A, van Gorsel E, Vogt R (2007) Coherent structures in urban roughness sublayer turbulence. Int J Climatol 27:1955–1968. https://doi.org/10.1002/joc.1625

Denby B (1999) Second-order modelling of turbulence in katabatic flows. Boundary-Layer Meteorol 92:67–100

Dupont S, Brunet Y (2008) Influence of foliar density profile on canopy flow: a large-eddy simulation study. Agric For Meteorol 148:976–990

Dupont S, Patton EG (2012) Influence of stability and seasonal canopy changes on micrometeorology within and above an orchard canopy: the CHATS experiment. Agric For Meteorol 157:11–29. https://doi.org/10.1016/j.agrformet.2012.01.011

Emmel C (2014) Vertical distribution of carbon dioxide, water vapour, momentum and energy exchange within and above a forest stand affected by the mountain pine beetle. Ph.D. thesis, University of British Columbia. https://doi.org/10.14288/1.0072175

Everard K (2017) On nighttime turbulent exchange within and above a sloped vineyard. Master's thesis, University of British Columbia https://doi.org/10.14288/1.0353181

Finnigan J (2000) Turbulence in plant canopies. Ann Rev Fluid Mech 32(1):519–571

Finnigan JJ, Shaw RH, Patton EG (2009) Turbulence structure above a vegetation canopy. J Fluid Mech 637:387–424. https://doi.org/10.1017/S0022112009990589

Fleagle RG (1950) A theory of air drainage. J Meteorol 7:227–232

Francone C, Katul G, Cassardo C, Richiardone R (2012) Turbulent transport efficiency and the ejection-sweep motion for momentum and heat on sloping terrain covered with vineyards. Agric For Meteorol 162–163:98–107

Gao W, Shaw R et al (1989) Observation of organized structure in turbulent flow within and above a forest canopy. Boundary-Layer Meteorol 47(1–4):349–377

Garrett A (1983) Drainage flow prediction with a one-dimensional model including canopy, soil and radiation parameterizations. J Clim Appl Meteorol 22:79–91

Grachev AA, Leo LS, Sabatino SD, Fernando HJS, Pardyjak ER, Fairall CW (2016) Structure of turbulence in katabatic flows below and above the wind-speed maximum. Boundary-Layer Meteorol. https://doi.org/10.1007/s10546-015-0034-8

Gudiksen P, Leone J Jr, King C, Ruffieux D, Neff W (1992) Measurements and modeling of the effects of ambient meteorology on nocturnal drainage flows. J Appl Meteorol 31(9):1023–1032

Horst T, Doran J (1986) Nocturnal drainage flow on simple slopes. Boundary-Layer Meteorol 34:263–286

Horst TW, Doran JC (1988) The turbulence structure of nocturnal slope flow. J Atmos Sci 45(4):605–616

Irvine MR, Gardiner BA, Hill MK (1997) The evolution of turbulence across a forest edge. Boundary-Layer Meteorol 84(3):467–496. https://doi.org/10.1023/A:1000453031036

Jacobs A, Van Boxel J, El-Kilani R (1994) Nighttime free convection characteristics within a plant canopy. Boundary-Layer Meteorol 71(4):375–391. https://doi.org/10.1007/BF00712176

Klipp C (2018) Turbulent friction velocity calculated from the Reynolds stress tensor. J Atmos Sci 75(4):1029–1043. https://doi.org/10.1175/JAS-D-16-0282.1

Launiainen S, Vesala T, Mölder M, Mammarella I, Smolander S, Rannik Ü, Kolari P, Hari P, Lindroth A, Katul GG (2007) Vertical variability and effect of stability on turbulence characteristics down to the floor of a pine forest. Tellus B Chem Phys Meteorol 59(5):919–936

Leclerc MY, Beissner KC, Shaw RH, Hartog GD, Neumann HH (1990) The influence of atmospheric stability on the budgets of the Reynolds stress and turbulent kinetic energy within and above a deciduous forest. J Appl Meteorol 29:916–933

Lee X, Barr AG (1998) Climatology of gravity waves in a forest. Q J R Meteorol Soc 124(549):1403–1419

Li D, Bou-Zeid E (2011) Coherent structures and the dissimilarity of turbulent transport of momentum and scalars in the unstable atmospheric surface layer. Boundary-Layer Meteorol 140:243–262. https://doi.org/10.1007/s10546-011-9613-5

Liss K, Leitch A, Christen A (2009) Sonic anemometer field inter-comparison, internal report. Technical report, The University of British Columbia

Mahaffee WF, Stoll R (2016) The ebb and flow of airborne pathogens: monitoring and use in disease management decisions. Phytopathology 106(5):420–431

Mahrt L (1982) Momentum balance of gravity flows. J Atmos Sci 39:2701–2711

Miller NE, Stoll R, Mahaffee WF, Neill TM, Pardyjak ER (2015) An experimental study of momentum and heavy particle transport in a trellised agricultural canopy. Agric For Meteorol 211:100–114

Miller NE, Stoll R, Mahaffee WF, Pardyjak ER (2017) Mean and turbulent flow statistics in a trellised agricultural canopy. Boundary-Layer Meteorol. https://doi.org/10.1007/s10546-017-0265-y

Oke TR, Mills G, Christen A, Voogt JA (2017) Urban climates. Cambridge University Press, Cambridge

Oldroyd H, Katul G, Pardyjak E, Parlange M (2014) Momentum balance of katabatic flow on steep slopes covered with short vegetation. Geophys Res Lett 41:4761–4768

Oldroyd HJ, Pardyjak ER, Higgins CW, Parlange MB (2016) Buoyant turbulent kinetic energy production in steep-slope katabatic flow. Boundary-Layer Meteorol 161(3):405–416

Pan Y, Patton EG (2017) On determining stationary periods within time series. J Atmos Ocean Technol 34(10):2213–2232

Poggi D, Katul G (2007) The ejection-sweep cycle over bare and forested gentle hills: a laboratory experiment. Boundary-Layer Meteorol 122:493–515. https://doi.org/10.1007/s10546-006-9117-x

Poggi D, Katul GG (2008) Micro- and macro-dispersive fluxes in canopy flows. Acta Geophys 56(3):778–799. https://doi.org/10.2478/s11600-008-0029-7

Poggi D, Porporato A, Ridolfi L, Albertson J, Katul G (2004) The effect of vegetation density on canopy sub-layer turbulence. Boundary-Layer Meteorol 111(3):565–587

Raupach M (1981) Conditional statistics of Reynolds stress in rough-wall and smooth-wall turbulent boundary layers. J Fluid Mech 108:363–382

Raupach MR, Antonia RA, Rajagopalan S (1991) Rough-wall turbulent boundary layers. Appl Mech Rev 44(1):1–24

Raupach MR, Finnigan JJ, Brunet Y (1996) Coherent Eddies and Turbulence in Vegetation Canopies: The Mixing-Layer Analogy. Boundary-Layer Meteorol 78:351–382

Shaw R, Tavangar J, Ward D (1983) Structure of the Reynolds stress in a canopy layer. J Clim Appl Meteorol 22:1922–1931

Shaw R, Brunet Y, Finnigan J, Raupach M (1995) A wind tunnel study of air flow in waving wheat: two-point velocity statistics. Boundary-Layer Meteorol 76:349–376

Stiperski I, Rotach MW (2016) On the measurement of turbulence over complex mountainous terrain. Boundary-Layer Meteorol 159(1):97–121. https://doi.org/10.1007/s10546-015-0103-z

Thomas C (2011) Variability of sub-canopy flow, temperature, and horizontal advection in moderately complex terrain. Boundary-Layer Meteorol 139:61–81

Thomas C, Foken T (2007a) Flux contribution of coherent structures and its implications for the exchange of energy and matter in a tall spruce canopy. Boundary-Layer Meteorol 123(2):317–337

Thomas C, Foken T (2007b) Organised motion in a tall spruce canopy: temporal scales, structure spacing and terrain effects. Boundary-Layer Meteorol 122(1):123–147

Tritton DJ (2012) Physical fluid dynamics. Springer, Berlin. https://doi.org/10.1007/978-94-009-9992-3

Turnipseed AA, Anderson DE, Blanken PD, Baugh WM, Monson RK (2003) Airflows and turbulent flux measurements in mountainous terrain: part 1. Canopy and local effects. Agric For Meteorol 119(1):1–21. https://doi.org/10.1016/S0168-1923(03)00136-9

Vickers D, Mahrt L (2006) A solution for flux contamination by mesoscale motions with very weak turbulence. Boundary-Layer Meteorol 118(3):431–447

Volino RJ, Simon TW (1994) An application of octant analysis to turbulent and transitional flow data. Trans Am Soc Mech Eng J Turbomach 116:752–752

Whiteman CD (2000) Mountain meteorology. Oxford University Press, Oxford

Wilks DS (2011) Cluster analysis. In: International geophysics, vol 100. Elsevier, pp 603–616